Lasers in Manufacturing Conference 2019

Liquid zone and spatter behavior during continuous laser welding of titanium

I. Tomashchuk[a*], A. Chabot[b], P. Cottet[b], M. Duband[a], P. Sallamand[a], A. Mannucci[a,c]

[a]*Laboratoire Interdisciplinaire Carnot de Bourgogne, UMR CNRS-6303, Université de Bourgogne-Franche Comté, 12 rue de la Fonderie, 71200 Le Creusot, France*
[b]*IUT Le Creusot, Mesures Physiques, 12 rue de la Fonderie, 71200 Le Creusot, France*
[c]*SME Laser Rhône-Alpes, 49-51 Boulevard Paul Langevin, 38600 Fontaine, France*

Abstract

Welding lines were performed on 2 mm thick titanium plates with continuous Yb:YAG laser with 600 µm spot diameter and different combinations of laser power (1-5 kW) and speed (1-12 m/min). High-speed imaging was performed with a camera Phantom V9.0 with the use of interferential filter of 810 nm to visualize only self-illuminated melted zone.
The observed welding regimes were close to those previously reported for steel: regular Rosenthal regime with and without spatter, smooth spatter-free single wave regime, quite unstable elongated keyhole regime and low energy conduction regime. Unlike steel, the noticeable change in the morphology of weld crosscuts was not observed, but a simple reduction of weld width with a decrease of linear energy. Important spatter formation occurred only for Rosenthal regime under P≥2kW. The analysis of spatter size and speed showed the relation between laser power and population of tiny, average and giant droplets with speed from 3.5 to 0.5 m/s.

Keywords: laser welding; titanium; keyhole regime; spatter; high-speed imaging.

1. Introduction

Numerous experimental studies were dedicated to the comprehension of formation and behavior of the keyhole generated by high power laser beam on metallic materials (Fabbro, 2013). However, number of works dedicated to the behavior of spatter in laser welding remains little and most of them treat the case of

* Corresponding author. Tel.: +33-3-85-73-11-23; fax: +33-3-85-73-11-20.
E-mail address: iryna.tomashchuk@u-bourgogne.fr.

stainless steels welded by Nd:YAG lasers.Recent progress in spatter observation was highly promoted by the increase in accessibility of high-speed imaging and by the development of image analysis tools allowing analyzing an important amount of data related to individually emitted droplets. Kaplan and Powell, 2011 described the mechanisms of spatter formation during continuous laser welding involving local boiling, acceleration of the melt and accumulation of vertical momentum and proposed the relation between droplet size and velocity. Weberpals and Dausinger, 2007, demonstrated the influence of welding parameters on spatter formation and ejection angle and proposed the forward inclination of the laser source to reduce the number of spatters. They reported chaotic ejection angle for low welding speeds (<6 m/min) and the linear increase of rear ejection angle with more elevated speeds. Schweier et al, 2013, proposed object-tracking algorithm to quantify the effect of beam oscillation and other operational parameters on spatter emission. Okamoto et al, 2012, proposed stereo-configuration with two high-speed cameras allowing to follow 3D movements of the droplets and providing statistical treatment of data by establishing the histograms describing speed and velocity of spatters. Zhang et al, 2013, made important advances in comprehension of the different spatter emission mechanisms by directly observing the movements of keyhole wall through glass window in case of high power and low speed welding: front ejection of large and relatively slow (several m/s) droplets from front keyhole wall and splashing of the liquid metal at the rear of unstable keyhole wall under action of strong vapor plume bursts. They considered viscous friction drag force the main cause of spatter emission in full penetration welding. You et al, 2014, proposed a high-speed visual detection method for online monitoring of welding quality though the processing of values of grey scale of spatters. Li et al, 2014, combined high-speed imaging and X-ray transmission imaging system to investigate the relationships between spatter formation, behavior of the melt and seam shape. They reported increase of spattering proportional to laser power and the variation of spatter emission mechanisms depending on the defocusing of the beam, with lesser mass loss in case of focal position inside the plate. Schweier et al, 2016, used automated spatter tracking for statistical representation of ejection mechanisms, spatter width and velocity in case of oscillated laser beam welding of steel. They reported the most frequent size of spatters of about 70 µm and the most frequent velocity of several m/s. Wu et al, 2017, proposed a multiphysical numerical model able to predict various ejection mechanisms for laser welding of aluminum alloy that was in accordance with phenomenology previously observed by Zhang et al, 2013 on steel.

Laser welding of titanium and titanium alloys find various applications in transport, chemical and other industries. However, little investigations of spattering were reported. Nakamura et al, 2015, studied spatter formation on 10-20 mm thick pure titanium during low speed continuous welding with 10 kW Yb:YAG laser, by combination of high speed imaging and X-ray imaging with use of tungsten carbide tracers. They reported that the location of spatter emission was shifting with the increase of welding speed from front ejection to lateral and then to rear ejection, and associated larger spatters to lower welding speeds. Nakamura et al, 2015, concluded that titanium is more sensible to spattering than stainless steel, because the forward inclination of the keyhole did not result in suppression of spatters. The tracing of trajectories of WC particles showed the involvement of the liquid past the keyhole in large vortex with velocity 0.53 m/s, the acceleration on rear keyhole wall up to 1.56 m/s right before the formation of ~1 mm sized droplet, flight acceleration up to 2.1 m/s and progressive deceleration before landing in front of the keyhole.

The present study is dedicated to the comprehension of melted zone and spatter behavior in case of full penetration continuous Yb:YAG laser welding of 2 mm thick commercially pure titanium over wide range of operational parameters, to cover different zones of keyhole and spatter behaviors.

2. Experiment

Welding lines were performed on 2 mm thick titanium plates with continuous Yb:YAG laser with 600 µm spot diameter and different combinations of laser power (1-5 kW) and speed (1-12 m/min). In all experiments, the laser beam was focused on the top surface of the plate. Argon was used as protection gas with debit of 20 l/min.

High-speed imaging was performed with the camera Phantom V9.0 with the use of the interferential filter of 810 nm to visualize only self-illuminated melted zone. In the first place, lateral observation with the camera inclined at horizontal 60° was performed (Figure 1a). The self-illumination of the melted zone allows better view of keyhole opening and associated fluid dynamics, as well as of ejection of spatters, comparing to frequently used (Tomashchuk et al, 2017) external illumination by diode laser (Figure 1b,c). In additional experiments, diode laser illumination was used for top observation of bottom keyhole opening, and the camera was fixed on the welding head with vertical angle of 5°.

Polished and etched with Keller reagent cross-sections of the welds and raw weld surfaces were observed with optical microscopy.

High-speed images were hand-processed with the software Phantom Media Player and Mesurim Pro. The size of the spatter was calculated using the comparison between the dimensions of the droplets landed outside of the melted zone visible on the video (in px) and the same droplets measured on the top-view of the weld (in µm). The velocity of droplets U_d was calculated from longitudinal (Δx) and vertical (Δz) displacement between two successive images separated by the time lapse Δt of 2 ms:

$$U_d = \sqrt{U_x^2 + U_z^2} = \sqrt{\left(\frac{\Delta x}{\Delta t}\right)^2 + \left(\frac{\Delta z}{\Delta t}\right)^2} \quad (1)$$

As the droplets are mainly ejected from the front and rear wall of the keyhole, the orientation of the camera perpendicularly to the welding direction allows adequate estimation of the spatter velocity in the joint plane. However, this simple method underestimates the velocity of the spatter that is ejected with some angle to welding axis. Top view observation of spattering confirmed preferential ejection close to joint axis.

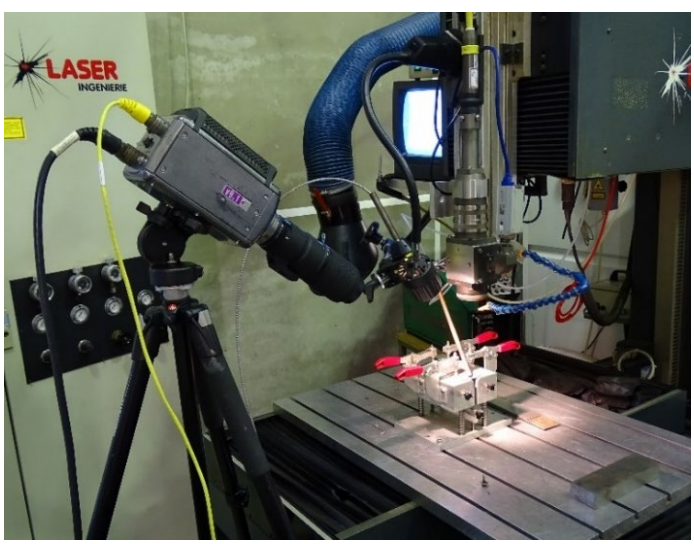

(a)

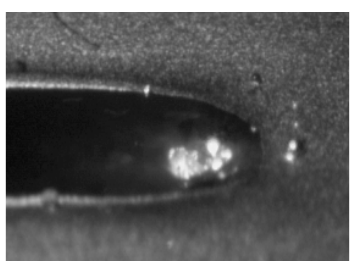

(b)

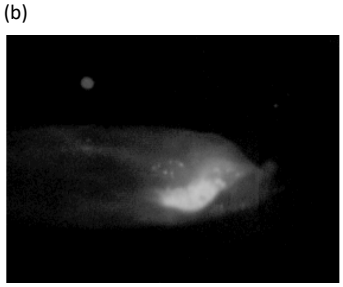

(c)

Fig. 1**.** Configuration of the experiment (a); comparison of lateral view of melted zone with (b) and without (c) additional illumination with 810 nm diode laser (P = 3 kW, V = 3 m/min).

3. Results and discussion

3.1. Observed welding regimes and keyhole inclination

The identified welding regimes were similar to those previously described by Fabbro, 2013, for stainless steel. However, the windows of corresponding operational parameters were found slightly different for titanium (Table 1). Low speed welds with linear energy $E_l \geq$ 30 kJ/m corresponded to Rosenthal regime, characterized by the circular opening of the keyhole, chaotic ejection of spatters and flat melted zone past the keyhole (Figure 2.a). Low laser power (1 kW) resulted in Rosenthal regime free of spatters. The increase of welding speed led to the transition to single wave regime mostly free of spatters and characterized by the presence of stable swelled wave at the back of the circular keyhole opening (Figure 2.b). The combination of maximal laser power (5 kW) and maximal welding speed (10-12 m/s) resulted in quite unstable elongated keyhole regime with lateral ejection of liquid veins, a phenomenon that was not observed for steel (Figure 2.c). Low linear energies resulted in keyhole-free conduction regime. Complete or partial penetration of the welds did not depend only on linear energy, but also on the associated welding regime.

Table 1**.** The mapping of observed welding regimes and associated linear energy.

***E_l=P/V* (kJ/m)**	V (m/min)							
P (kW)	1	2	3	4	6	8	10	12
5	300	150	100	75	50	37.5	30	25
4	240	120	80	60	40	30	24	20
3	180	90	60	45	30	22.5	18	15
2	120	60	40	30	20	15	12	10
1	60	30	20	15	10	7.5	6	5

Rosenthal with no spatters
Rosenthal with spatters
Single wave
Unstable elongated keyhole
Conduction mode

In black : full penetration
In white : partial penetration

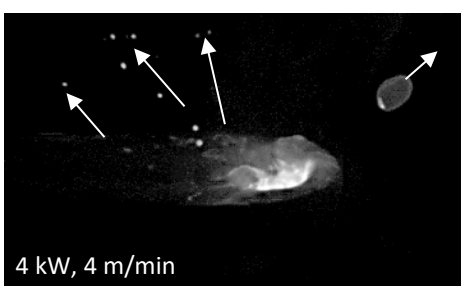

(a)

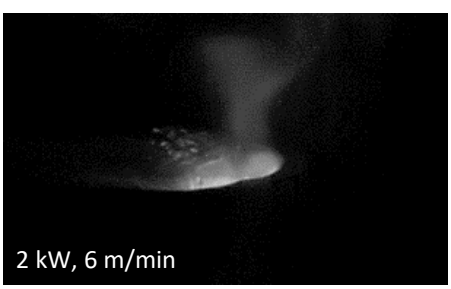

(b)

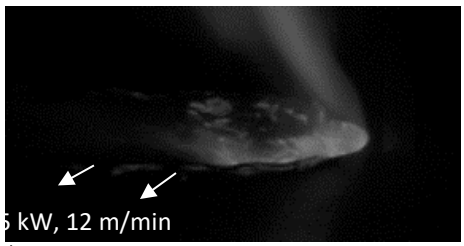

(c)

Fig. 2. Identified welding regimes: Rosenthal (a), single wave (b) and unstable elongated keyhole (c).

Top observation of the keyhole allows estimating the inclination of the front wall by measuring the shift between top and bottom openings (Fabbro et al, 2005). Presuming the keyhole opening identical to the diameter of laser beam, in case of 2 mm thick plate and 600 µm wide laser spot, the bottom opening of the keyhole remains visible up to the inclination of about 17° (or tan α = *dl/h* = 0.306). Fabbro, 2013 gives the relation between linear energy of welding and the inclination of front wall of the keyhole (equation 2):

$$E_l = \frac{P}{V} = \frac{\pi Ø^2}{2kA_0 tan\ \alpha} = K\frac{Ø^2}{tan\ \alpha} \quad (2)$$

where P – laser power (W), V – welding speed (m/s), Ø – laser spot diameter (m), k and K – material dependent constants, A_0 – adsorption coefficient of laser radiation and α - inclination angle of front wall of the keyhole determined from the ratio of *dl* and plate thickness *h* (Figure 3.a). The measurements of keyhole inclination for laser powers of 2-4 kW and welding speed of 1-4 m/min allowed to estimate the constant K from the slop of linear fit of experimental values (Figure 3.b) and to perform the calculation of inclination angles for all experimental conditions given in Table 1, except the conduction regime, where keyhole inclination value has no meaning. The calculated inclination angles (Table 2) indicate that the transition from Rosenthal to single wave regime occurs around 13°, which is close to 15° reported by Fabbro, 2013 for stainless steel. The value of K for titanium is close to the value found for steel: $2 \cdot 10^{10}$ J/m^3 and $4 \cdot 10^{10}$ J/m^3 respectively. The zone of unstable elongated keyhole regime seems different from stable elongated keyhole regime reported for steel for welding speeds 9-11 m/min, and the associated inclination of keyhole front wall remains moderate compared to 30° reported by Fabbro, 2013.

Table 2. The calculated inclination angles of front keyhole wall.

α°	V (m/min)							
P (kW)	1	2	3	4	6	8	10	12
5	1.4	2.7	4.1	5.5	8.2	10.9	13.5	16.1
4	1.7	3.4	5.1	6.8	10.2	13.5	16.7	19.8
3	2.3	4.6	6.8	9.1	13.5	17.7	21.8	25.6
2	3.4	6.8	10.2	13.5	19.8	25.6		
1	6.8							

Rosenthal with no spatters
Rosenthal with spatters
Single wave
Unstable elongated keyhole
Conduction mode

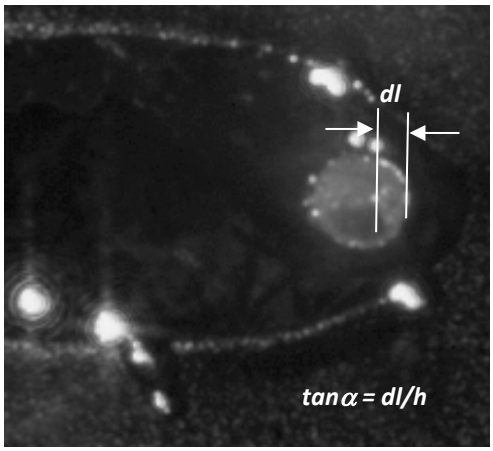

P = 3 kW, V = 3 m/min
(a)

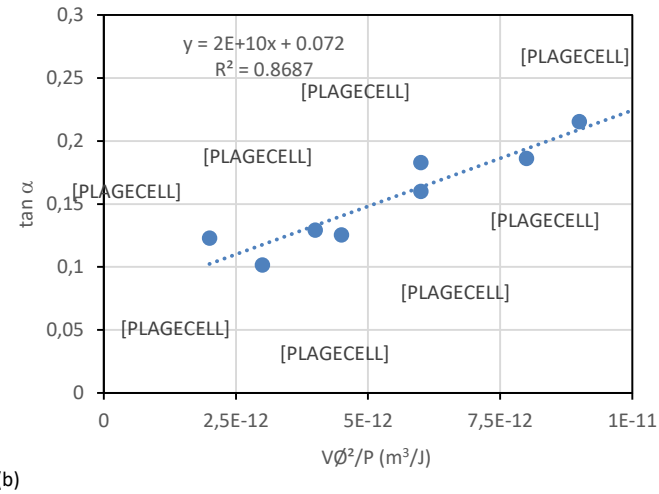

(b)

Fig. 3. Determination of inclination angle of front keyhole wall (a) and estimation material-dependent coefficient K (b).

3.2. Weld shape evolution

The melted zones in titanium did not show sharply distinct morphologies between different welding regimes. Highly energetic welds with Rosenthal regime resulted in thick melted zones with well-pronounced hourglass shape attributed to Marangoni convection (Figure 4.a). The increase of welding speed led to the progressive transition to the nail shape (Figure 4.b). The top surfaces of the welds performed in Rosenthal regime were regular and presented the traces of spatters. Single wave regime also had a nail shape, but with lower widths (Figure 4.c). The top surfaces of the welds were slightly wavy with little or no spatter. Unstable elongated keyhole regime was associated with a cup shape with pre-hump visible at the top of the weld (Figure 4.d). In this regime, the penetration of the melt presented periodic fluctuations. The top surface of such welds had very disturbed aspect due to the pronounced lateral projection of the liquid. For all operational conditions, the refinement of melted zone was proportional to the decrease of linear energy.

2 kW, 1 m/min
(a)

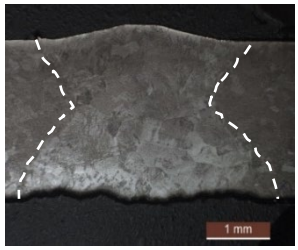

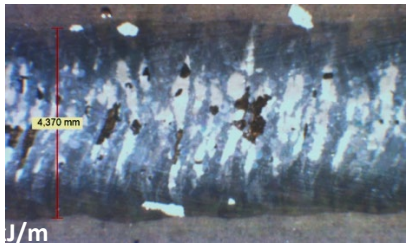

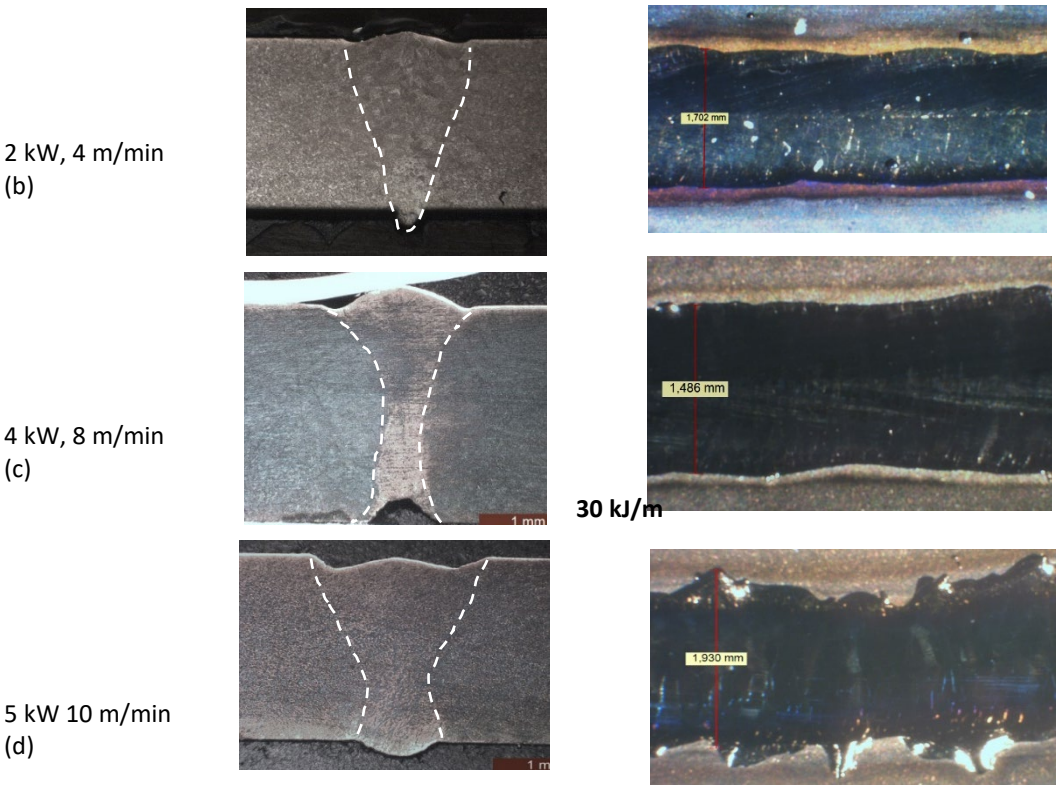

Fig. 4**.** Typical melted zones and weld surfaces**:** Rosenthal (a-b), single wave (c) and unstable elongated keyhole (d).

3.3. Behavior of the plume

As in the case of stainless steel (Fabbro et al, 2006), the sufficient increase of welding speed led to the noticeable rear inclination of the vapor jet from the keyhole (Figure 5). However, compared to the results reported for steel, the start of the inclination occurred at much higher speeds (≥ 8 m/min), associated to single wave and unstable elongated keyhole regime, which indicates tardive opening of the rear wall of the keyhole (Figure 5.b) in titanium. Moreover, the inclination of the plume had a tendency to stagnate before the transition from 68° to 54° for welding condition of 3 kW and 15 m/min that corresponds to the inclination of keyhole front wall of 31° (equation 2). According to Fabbro, 2013, the angle of keyhole wall of 30° marks the beginning of elongated keyhole regime. However, the melted zone still behaved like a single wave regime with keyhole opening close to circular. This once again underlines the difficulty of the opening of rear keyhole wall on titanium compared to steel. This difference may be related to lower recoil pressure of metallic vapor inside the keyhole in titanium, insufficient to open the rear wall of the keyhole. According to Kaidalov, 2004, at 3500 K, the recoil pressure of pure Ti is ten times lower than recoil pressure of pure Fe. Fabbro, 2013 stated that for steel the deviation of the plume can be used for the estimation of the inclination of keyhole wall. However, for titanium such attempts led to the values overestimated by 50%, because the rear wall of the keyhole strongly modifies the direction of vapor jet.

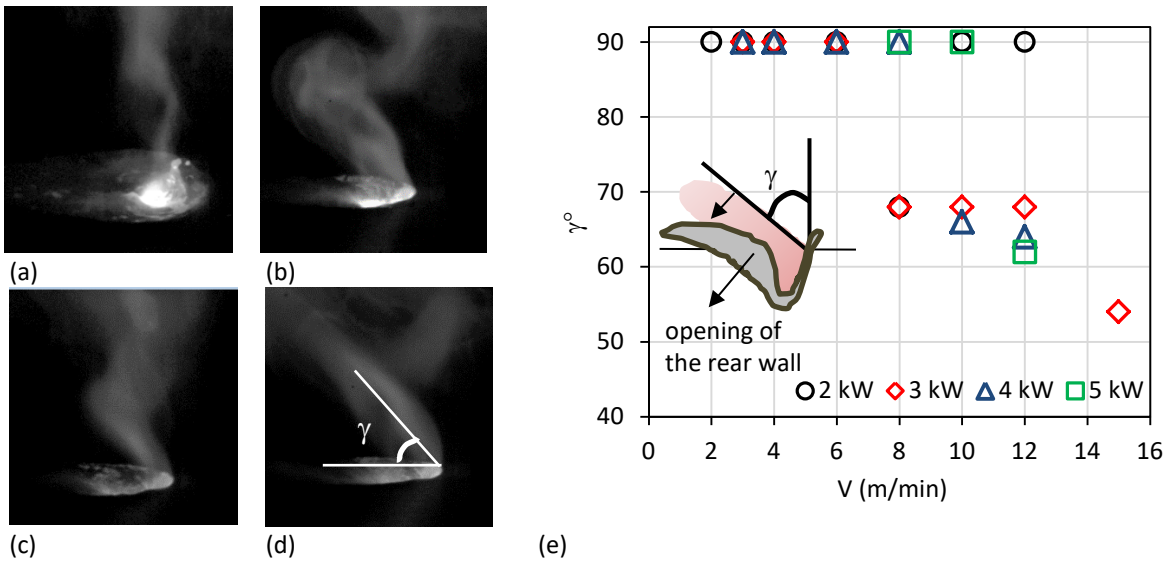

Figure 5**.** The progressive inclination of the plume at 6 (a), 8 (b), 10 (c), 15 (d) m/min (P = 3 kW) and the mapping of plume inclination in function of operational parameters (e).

3.4. Behavior of the spatters

According to Kaplan and Powell, 2011, the energy of ejected spherical droplet (E_{ej}) is composed by the kinetic and surface tension terms (equation 3).

$$E_{ej} \geq \rho_l \cdot \frac{U_d^2}{2} \cdot \frac{4\pi R_d^3}{3} + \sigma \cdot 4\pi {R_d}^2 \quad (3)$$

where ρ_l is the volume mass of liquid metal (kg/m^3), U_d is the initial velocity of spatter (m/s), R_d is the radius of spherical spatter (m) and is σ is the surface tension of liquid metal (N/m). In other terms, the ejection of the spatter becomes possible when the liquid pressure satisfies the following condition (equation 4):

$$p_{liq} \geq \rho_l \cdot \frac{U_d^2}{2} + \frac{3\sigma}{R_d} \quad (4)$$

The pressure in the liquid, on the keyhole walls p_{liq} can be approximated to the temperature-dependent recoil pressure of saturated metal vapor corrected by the condensation coefficient β (equation 5) (Hirano et al, 2012)

$$p_{recoil} = \frac{(1+\beta)}{2} \quad (5)$$

where A and B are the material-dependent constants.

Using the equation 4, the relation between the velocity and the radius of ejected droplets can be expressed as follows (equation 6):

$$U_d \leq \sqrt{\frac{2p_{liq}}{\rho} - \frac{6\sigma}{\rho}} \quad (6)$$

The linearized form of equation 6 allowed estimating the values of minimal relative pressure on the keyhole walls and minimal temperature of ejected liquid (Table 3) by tracing the $U_d^2 = f(1/R_d)$ line tangent to the totality of experimental points (Figure 6.a). Accordingly, the theoretical curve $U_d = f(R_d)$ was superposed with experimental data (Figure 6.b).

Table 3. Estimated liquid pressure and temperature and the constants used for tracing $U_g = f(R_g)$ curve.

Estimated values		Constants used for the estimation				
p_{liq} (Pa)	T_{liq} (K)	A	B (K)	ρ (kg/m^3)	β	σ (N/m)
8190	3150	6.358	-22747	3865	0.5	1.39

The distribution of experimental values was well described by equation 6, with zone of authorized values of speed under the $U_d = f(R_d)$ curve and empty zone above it (Figure 6.b). Minimal relative pressure resulting in spatter ejection was estimated to ~8 kPa, and minimal temperature of liquid – to 3150 K. The minimal detectable size of spatter considered as 2x2px corresponds to the radius of 14 µm. Minimal radius of detected spatter was of 28 µm, which is close to the value of 42 µm reported by Schweier et al, 2016, and the maximal radius reached 400 µm. The associated maximal velocities of droplets were of 4 m/s down to 0.1 m/s, which is comparable with results of Nakamura et al, 2015. As the velocity of spatters was calculated by comparison of two or more successive images, the maximal detected velocity of spatter was limited by the size of the observation zone and by fixed frequency of images. If the melted zone is situated roughly in the center of the observation zone (Figure 6.b), and the spatter moves from the center along the semi-diagonal of 720 px (or 9.69 mm), the fixed frequency of images will not allow to detected the spatter more rapid than 4 m/s, which corresponds to the maximal experimental velocities. This means that the maximal velocities of smallest spatter were possibly underestimated by 1-2 m/s and can attain ~6 m/s. For the slowest spatters, the observation on several consecutive images allowed to estimate the acceleration of ~40 m/s².

The important dispersion of observed velocities of spatter can be attributed to following factors:

- fluctuation of temperature and pressure of the ejected liquid
- probabilistic fragmentation of liquid film and flying droplets
- different flight times during the capture of images, as the droplets have noticeable acceleration
- underestimation of speed of the droplets that are ejected in the direction of the camera.

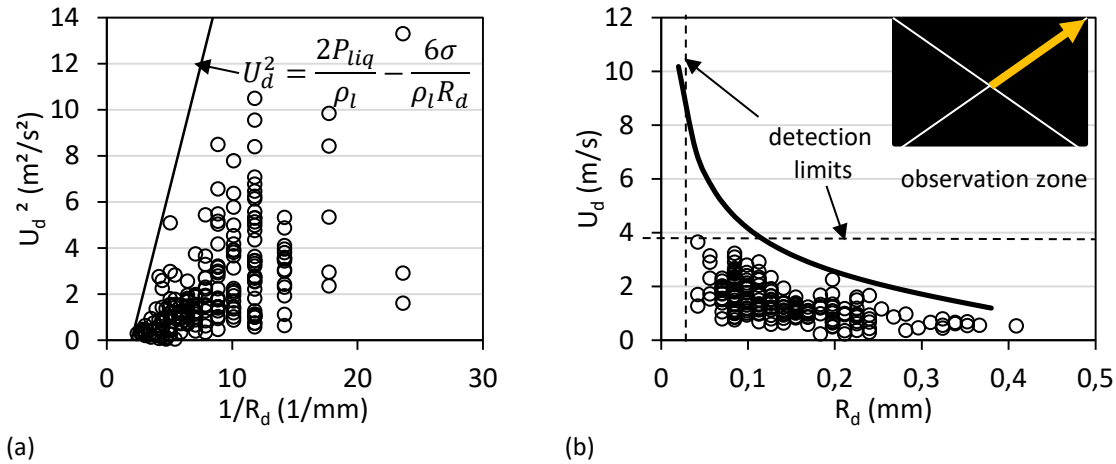

Fig. 6. Theoretical relation between droplet radius and velocity compared with experimental data from all welds.

The ejection of the spatters occurred through three main mechanisms that depend on welding regime and linear energy (Table 4): front, rear and lateral ejection. Front ejection of large droplets (Figure 7.a and Figure 2.a), previously reported by Zhang et al, 2013, was explained by Nakamura et al, 2015 as a phenomenon of rise of the liquid along front wall of the keyhole, promoted by the expanding vapor jet. Naturally, this type of spatters disappears at high welding rates, when the thickness of liquid in front of the keyhole becomes insignificant. This type of spatter was limited to the Rosenthal regime. The rear ejection of the clusters of little droplets (Figure 7.b and Figure 2.a) is explained by the rise of liquid wave along rear wall of the keyhole and the following fragmentation under burst of recoil pressure (Zhang et al, 2013). Rear projection is very pronounced in Rosenthal regime and becomes less important in other regimes, but with the increase of welding speed, it disappears only after front ejection, because of the bigger volume of moving liquid at the rear of the keyhole. According to Fabbro, 2013, rear ejection is the main type of spatters in single wave regime. Lateral ejections were very pronounced in the unstable elongated keyhole regime, but also existed in neighboring conditions of single wave regime. Some part of single wave regime and conduction regime are free of spatters, but these less energetic conditions are associated with partial penetration.

Table 4**.** The mapping of different mechanisms of spatter ejection.

	V_s (m/min)							
P (kW)	1	2	3	4	6	8	10	12
5	FR	FR	FR	FR	FR	fr	rL	L
4	FR	FR	FR	FR	fr	rl	rl	l
3	FR	FR	FR	FR	fr	r	r	
2	FR	FR	FR					
1								

F	Important front ejections
R	Important rear ejections
L	Important lateral ejections
f	Rare front ejections
r	Rare rear ejections
l	Rare lateral ejections

For the significance of colors, see Table 1.

The angle of spatter ejection reflects the behavior of the keyhole (Weberpals and Dausinger, 2008).

During front ejection of spatters (Figure 7.a), the angle of ejection φ decreases with welding speed (Figure 6.b), linearly to the reduction of the vapor pressure in the keyhole, that is responsible for the upward momentum of spatter, in agreement with conclusions of Wu et al, 2017. Rear ejection angle ε (Figure 7.b) stagnates at low welding speeds and decreases in the single wave regime because of proportional opening of rear keyhole wall (Figure 7.d). As long as the keyhole exists, angle ε is not very sensible to variation of laser power, but depends strongly on the welding speed.

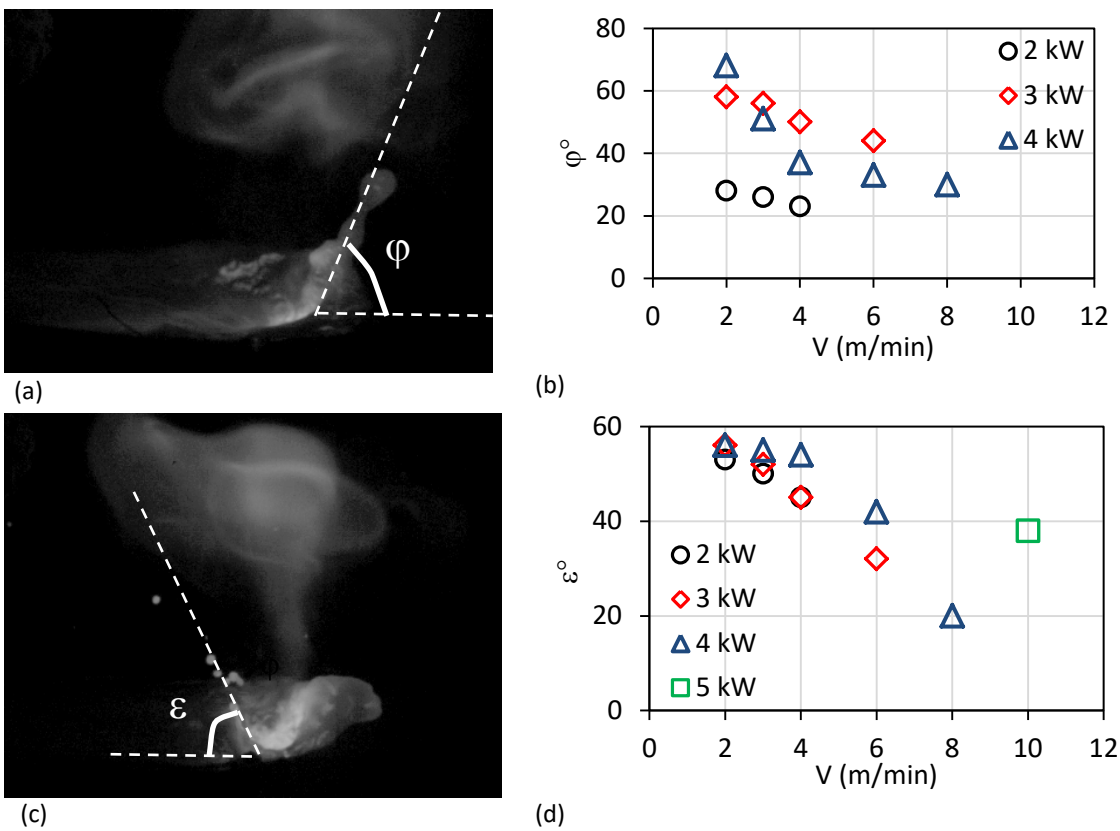

Fig. 7**.** Ejection of spatters from the front (a,b) and the rear keyhole walls (c,d).

Weberpals and Dausinger, 2008 established linear relationship between the angle of rear spatter and the inclination of front keyhole wall in stainless steel. In case of pure titanium (Figure 8), this relation is not linear: horizontal deviation of rear ejection of spatters decreases from 60° to 20° proportionally to the inclination of keyhole wall according to second-degree polynomial functions (dash lines) individual for each laser power. When the inclination of front wall exceeds 13°, rear spatter becomes marginal, and visible ~20° vertical deviation of vapor plume takes place. Vertical inclination of the plume is not observable at welding speeds < 8 m/min because the rear wall of the keyhole remains close to vertical, which explains high values of ε. The shift from Rosenthal to single wave regime occurs due to the opening of rear keyhole wall and stabilization of smooth liquid wave. It can be supposed that the progressive opening and smoothing of rear keyhole wall is reflected by the reduction of ε and further disappearance of rear spatter when the vertical

wall is replaced by smooth wave of liquid no longer subjected to random bursts of recoil pressure.

The population of spatters can be roughly divided into three groups: tiny (R_d<100 µm) rapid spatters, average spatters and giant (R_d >250 µm) slow spatters. Within Rosenthal regime, these populations show strong correlation with laser power. The population of tiny spatters emitted both from the front and the rear of the keyhole prevails under low laser power and becomes marginal at 4 kW (Figure 9.a). A contrario, giant droplets become marginal at low laser power and reach ~30% of total population at 4 kW (Figure 9.b).

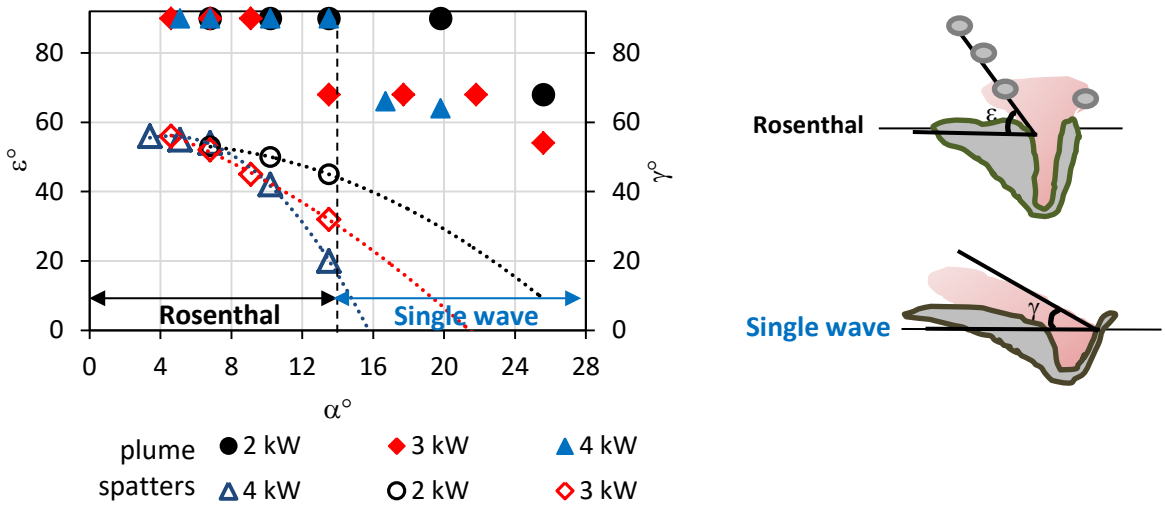

Fig. 8. The relation between the inclination of front keyhole wall and the angles of rear spatter (empty markers) and plume (filled markers).

4. Conclusions

Parametric study of melted zone and keyhole behavior during high power welding of commercially pure titanium showed the existence of welding regimes similar to those previously reported for stainless steel : regular Rosenthal regime with and without spatter, smooth spatter-free single wave regime, quite unstable elongated keyhole regime and low energy conduction regime. The shift from Rosenthal to single wave regime occurred at little higher welding rates compared to steel and was associated to the inclination of front keyhole wall of 13° creating opening and stabilization of the rear keyhole wall, associated with formation of smooth wave, decrease of ejection angle of rear spatters and progressive inclination of the plume. The opening of rear wall and elongation of the keyhole on titanium are difficult compared to steel because of lower recoil pressure of pure Ti. This is why the elongated keyhole regime is observed only at maximal laser powers, and is associated to very unstable behavior of the melted zone. Unlike steel, the noticeable change in the morphology of weld crosscuts was not observed, but simple reduction of weld width with decrease of linear energy, and eventual loss of penetration.

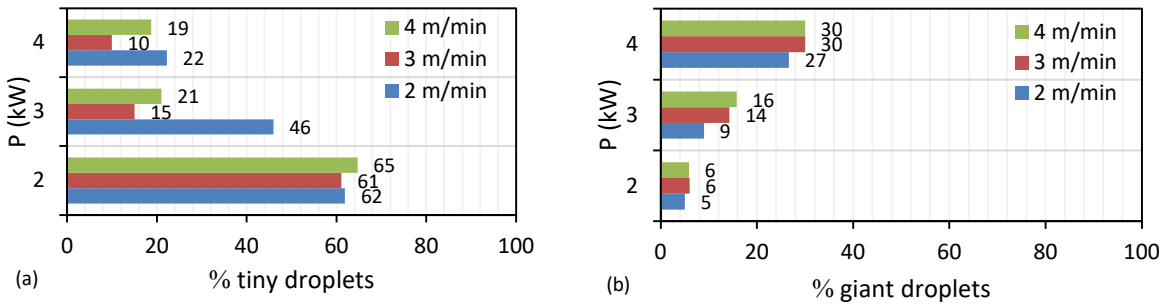

Fig. 9. Variation of populations of tiny (a) and giant (b) spatters in function of welding parameters.

Three mechanisms of spatter formation were observed: front ejection, proper to Rosenthal regime under P≥2kW, rear ejection, occurring in both Rosenthal and single wave regimes and lateral ejection, proper to unstable elongated keyhole regime. Lateral ejection of liquid veins that remain connected to the main melted zone, creates a very disturbed aspect of the top surface of the weld, otherwise smooth and regular.

The analysis of spatter size and speed showed the relation between laser power and a population of tiny, average and giant droplets with speed from 3.5 to 0.5 m/s. The increase of laser power induces the progressive reduction of a population of tiny rapid spatter and domination of average and giant spatters.

References

Fabbro R., Slimani S., Doudet I., Coste F., Briand F., 2005, Study of keyhole behaviour for full penetration Nd–Yag CW laser welding. J. Phys D : Appl. Phys. 38, p. 1881-1887.

Fabbro R., Slimani S., Doudet I., Coste F., Briand F., 2006, Experimental study of the dynamical coupling between the induced vapour plume and the melt pool for Nd–Yag CW laser welding. J. Phys. D : Appl. Phys. 39, p. 394-400.

Fabbro R. 2013, Developments in Nd:YAG laser welding in Handbook of laser welding technologies (Editor S. Katayama), Woodhead Publishing Limited, Oxford, pp. 47-72.

Hirano K., Fabbro R., Muller M., Study on temperature dependence of recoil pressure near the boiling temperature - Towards better modeling and simulation. ICALEO 2012 Congress Proceedings, p. 678-684.

Kaidalov, A.A., 2004, Electron beam welding and annexed technologies (in Russian), Technologia, Kyiv.

Kaplan A.F.H., Powell J., 2011, Spatter in laser welding. J. Laser Appl. 23, p.032005-1-03205-7.

Li S., Chen G., Katayama S., Zhang Y., 2014, Relationship between spatter formation and dynamic molten pool during high-power deep-penetration laser welding. Appl. Surf. Sci. 303, p. 481-488.

Okamoto Y., Yamamoto H., Okada A., Shirasaya K., Kohelmainen J.T., 2012, Velocity and angle of spatter in fine laser processing. Phys. Procedia 39, p. 792-799.

Nakamura H., Kawahito Y., Katayama S., 2015, Fundamental study for the relationship between melt flow and spatter formation in high-power laser welding of pure titanium. Trans. JWRI 44, p. 27-32

Schweier, M., Heins, J.F., Haubold, M.W., Zaeh, M.F., 2013, Spatter Formation in Laser Welding with Beam Oscillation. Phys. Procedia, 41, p.20-30.

Schweier, M., Heins, J.F., Haubold, M.W., Zaeh, M.F, 2016, Spatter Formation in Laser Welding with Beam Oscillation, Phys. Procedia 41, p.20-30.

Tomashchuk I., Mostafa M., Caudwell A., Sallamand P., Duband M., 2017, Behavior of laser induced keyhole during dissimilar welding of metals. Lasers in Manufacturing Conference 2017, Munich, Germany.

Weberpals J., Dausinger F., 2007, Influence of inclination angle on spatter behavior at welding with lasers of strong focusability. ICALEO 2007 Congress Proceedings, p. 858-865.

Weberpals J., Dausinger F., 2008, Fundamental understanding of spatter behavior at laser welding of steel. ICALEO 2008 Congress Proceedings, p. 364-373.

Wu D., Hua X., Li F., Huang L., 2017, Understanding of spatter formation in fiber laser welding of 5083 aluminum alloy. Internat. J. Heat Mass Trans. 113, p. 730-740.

You D., Gao X., Katayama S., 2014, Visual-based spatter detection during high-power disk laser welding, Opt. Laser Engineer. 54, p. 1-7.
Zhang, M.J., Chen, G.Y., Zhou, Y., Li S.C., Deng H., 2013, Observation of spatter formation mechanisms in high-power fiber laser welding of thick plate. Appl. Surf. Sci, 280, p.868-875.